Electric-dipole spin resonance and spin orbit coupling effects in odd-integer quantum Hall edge channels

A. V. Stier,[1,2] C. J. Meining,[1,*] V. R. Whiteside,[1] B. D. McCombe,[1] E. I. Rashba,[3] P. Grabs,[4] and L. W. Molenkamp[4]

[1]*Department of Physics, University at Buffalo, SUNY, Buffalo, New York 14260, USA*
[2]*Walter-Schottky Institut, Technische Universität München, 80333 München, Germany*
[3]*Department of Physics, Harvard University, Cambridge, Massachusetts 02138, USA*
[4]*Physikalisches Institut (EP3), Universität Würzburg, 97074 Würzburg, Germany*

(Received 22 September 2022; revised 22 November 2022; accepted 23 November 2022; published 4 January 2023)

We have observed remarkable multiple-line electron spin-resonance spectra in sensitive terahertz laser photoresponse measurements of the two-dimensional electron gas of an asymmetric InAs quantum well in the integer quantum Hall effect regime. Near filling factor 7 with the magnetic field oriented at large angles θ from the normal to the sample surface, rather than the expected single-electron spin-resonance line, we observed several sharp pairs of features at fields across the corresponding quantum Hall plateau. At a unique angle θ_c, the dominant central pair merges into a single line close to the estimated magnetic field of electron spin resonance. For $\theta > \theta_c$ this line splits into two sharper features whose separation in magnetic field increases with increasing θ. Surprisingly, for $\theta < \theta_c$ the central feature disappears. The explanation of this behavior, as well as the observation of additional pairs of sharp features with larger magnetic-field separations, is based on strong spin orbit coupling effects and the concomitant effective magnetic fields associated with pairs of oppositely directed, persistent quantum Hall edge currents combined with the behavior of edge channels near the center of the odd plateaus. Modeling the splitting of the spin resonances due to these effective spin orbit magnetic fields is in reasonable agreement with observations. These results show that it is possible to probe the widths of quantum Hall edge channels through the spectral specificity of the electron spin resonance and possibly manipulate spins with THz photons having wavelengths several orders of magnitude larger than the edge-channel widths.

DOI: 10.1103/PhysRevB.107.045301

I. INTRODUCTION

Spin orbit coupling and topology are two closely interconnected concepts in condensed matter physics. Topologically nontrivial phases in n dimensions are typically driven by spin orbit coupling induced band inversions, which result in the occurrence of $n-1$ dimensional "surface" channels. In two dimensions these are quasi-one-dimensional edge channels carrying a spin-polarized, dissipationless equilibrium current, protected from backscattering by symmetry. The edge channels of the integer quantum Hall effect [1–3] are an essential example of the importance of topological protection of such edge states. A significant development in this context was the prediction of a new class of topological states, topological insulators, and the connected quantum spin Hall effect, and their observation in HgTe quantum wells [4–7]. The connection between spin orbit coupling and topology has stimulated research in both fundamental and applied directions. On the one hand, the electron spin degree of freedom and/or the stability and chirality of one-dimensional (1D) topological channels may be exploited for developing new paradigms for electronic devices and information technology [8–12]. A key aspect in spintronics applications is the possibility of spin orbit coupling enabled spin manipulation via electric fields [13,14]. On the other hand, fundamental electronic parameters, such as the g factor and optical selection rules and oscillator strengths of electric-dipole transitions involving spin flips, depend strongly on spin orbit coupling (see, e.g., [15]). Studies of electron spin resonance in different frequency regions can provide important information about its strength and how it is affected by band structure and carrier density and, consequently, how strongly these properties affect other phenomena. For example, excitation of spins via electric fields, such as electric-dipole spin resonance (EDSR) and combined cyclotron–spin resonances [15], can provide easier access to probing and manipulating spins because of their much larger oscillator strength in materials with large spin orbit coupling. In this context HgTe, InSb, and InAs are especially interesting because of their large spin orbit coupling and the availability of quantum structures with excellent electronic properties.

In systems with fully formed one-dimensional edge channels, as in the integer quantum Hall effect for two-dimensional electron gases (2DEGs), or in the quantum spin Hall effect from inverted HgTe quantum wells, the location of the conducting channels is pinned close to the physical edges of the sample [16–22]. However, although the topological protection of the conductance quantization is beneficial in many cases, it makes the extraction of exact location and width of these edge channels impossible from standard magneto-transport measurements. Scanning probe measurements on

[*]Deceased.

GaAs 2DEGs have shown clear evidence of the edge channels in GaAs/(AlGa)As heterostructures [20,23–26] and graphene [21,27], but spatial resolution is limited. The present work, which combines topologically protected states in the integer quantum Hall effect with spin orbit induced magnetic fields, shows how spin-resonance measurements could provide detailed information about the formation and width of 1D edge channels.

Motivated initially by theoretical predictions [13,14] of strong electric-dipole spin resonance (EDSR) that is especially enhanced for large angles between applied magnetic field and the sample plane, we have made low-temperature magnetophotoresponse measurements on an InAs 2DEG in the integer quantum Hall regime. The parameter space investigated in our experiments encompasses the fields and tilt angles necessary to observe electron spin resonance estimated for the electron density and effective g factor of our sample. Unexpectedly, rather than the anticipated single-electron spin-resonance line, we observed multiline spectra, the central pair of which coalesces into a single line at a special tilt angle, θ_c, and *abruptly vanishes* for $\theta \leqslant \theta_c$. We attribute these unusual effects to local spin orbit coupling induced magnetic fields of electrons in distinct incompressible quantum Hall edge channels (QHECs) combined with the behavior of the edge channels with tilt angle and magnetic field. Furthermore, our studies show that it may be possible to manipulate spins localized in edge channels that are typically tens of nanometers in width, via high-frequency electric fields having wavelengths $\lambda > 100\,\mu$m that correspond to energies that are resonant with the effective spin splitting. This type of spin manipulation should also be possible in other examples of topologically protected quasi-one-dimensional channels with large spin orbit coupling.

Most investigations of the quantum Hall effect (including the extensive scanning probe studies referred to above) have focused on GaAs/(AlGa)As heterostructures and graphene mono- and multilayer structures due to their high quality, widespread availability, and interesting physics. However, the spin orbit coupling is relatively weak in these materials, e.g., in GaAs weak spin orbit coupling results in a small effective band g factor for electrons ($g^* = -0.44$); there have been few studies of the combined effect of spin orbit coupling and QHECs on spin resonance. We report here the results of our experimental low-temperature THz magnetophotoresponse measurements of electrons in a 2DEG of an InAs quantum well, which have a much larger single-particle conduction-band g value ($g^*_{sp} \approx -15$). The multiple lines appear in pairs, which suggests that these experiments selectively probe electron spins in specific QHECs through their spin resonance. We attribute the splitting of the line pairs to electron momentum dependent effective magnetic fields that result from spin orbit interaction generated by the local currents within the QHECs. These different effective fields lead to different total fields when combined vectorially with the applied magnetic field. The equilibrium counterpropagating currents in the edge channels produce equal and oppositely oriented spin orbit magnetic fields, $\mathbf{B}^{SO}$, in the plane of the 2DEG normal to the current direction. This allows one to assign different components of the spin multiplet to different channels, and to understand the dependence of the position and width of the resonant dips in photoresponse on the applied magnetic field **B**. The projection of B, $B_\perp = B\cos\theta$, determines the details of the quantum Hall effect and the widths of the edge channels, as well as the aforementioned vanishing of the single spin-resonance dip for $\theta < \theta_c$. We argue below that absence of any spin resonance for this case is due to vanishing of the edge channels for fields greater than that corresponding to filling factor $\nu = 7$. The large spin orbit interaction [28,29] and effective g factor of InAs both enhance selectivity. This spin orbit coupling originates, in general, from both structural and crystalline inversion asymmetries [30,31], but the former usually dominates in InAs and we ignore the latter in the remainder of this paper in the interest of simplicity.

Our experiments exploit the high sensitivity of the magnetotransport to changes in carrier temperature induced by resonant absorption of high-frequency radiation in the vicinity of the Zeeman energy [32–34], and thereby to investigate the widths of the QHECs (incompressible strips), which depend on their location relative to the edges across the width of the sample (Hall bar). The edge-channel locations depend upon the electrostatic depletion potential $V(x)$, with the x direction across the width of the sample, and the intersection of the resulting electron density dependence $n_s(x)$, with the density determined by the electrochemical potential in the 2D bulk (and compressible strips). Our discovery and its interpretation show that addressing and manipulating electron spins in different channels independently is possible because of the spectral specificity of the spin resonance associated with lateral position and spatial separation of the channels, which can be of the order of the Hall bar sample width.

II. EXPERIMENTAL DETAILS

The heterostructure studied is a 15 nm InAs quantum well sandwiched between two layers of $Al_{0.35}Ga_{0.65}Sb$ grown by molecular beam epitaxy along the [001] direction. The layered structure of the sample is shown schematically in Fig. 1. Although the sample is not intentionally doped, the InAs quantum well hosts a 2DEG of density n_s that results from pinning of the chemical potential due to surface states of the top $Al_{0.35}Ga_{0.65}Sb$ layer. The electron density can be varied from $<7 \times 10^{11}$ cm^{-2} to 10^{12} cm^{-2} through visible and infrared light illumination, and the low-temperature mobility of the 2DEG is approximately 3×10^5 cm^2/V s at 4.2 K.

This structure was processed by standard optical lithography and wet etching techniques into a large Hall bar geometry (shown schematically in the inset to Fig. 2(c). The dimensions of the Hall bar are as follows: length: 2 mm; width: 0.25 mm; separation between longitudinal contacts: 1.7 mm. The resulting Hall bar was mounted in the variable temperature insert of an Oxford Instruments optical-access 10 T superconducting magnet system with room-temperature and helium-temperature windows providing access to THz and/or visible optical beams propagating either parallel or perpendicular to the magnetic field. The sample was mounted in a holder that allows rotation such that the normal to the sample surface (and the plane of the 2DEG) could be varied with respect to the magnetic field **B** by an angle θ in the plane perpendicular to the long Hall bar axis.

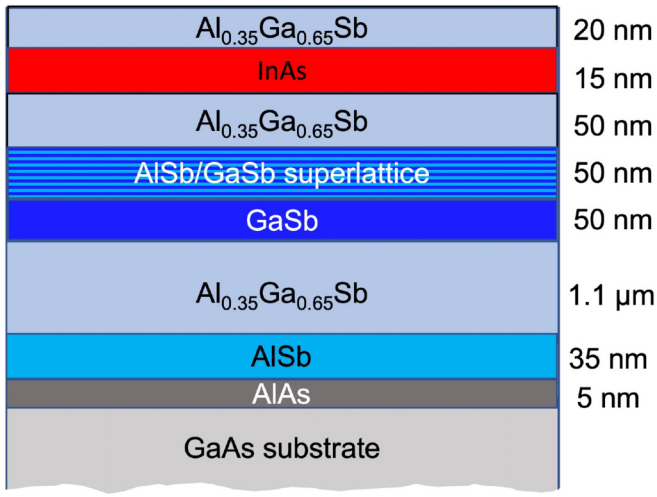

FIG. 1. Schematic diagram of the layered sample containing the InAs quantum well grown by molecular-beam epitaxy. The GaSb layer and the AlSb/GaSb superlattice are incorporated to trap impurities and optimize mobility of electrons in the InAs quantum well. N.B. The structure is not intentionally doped.

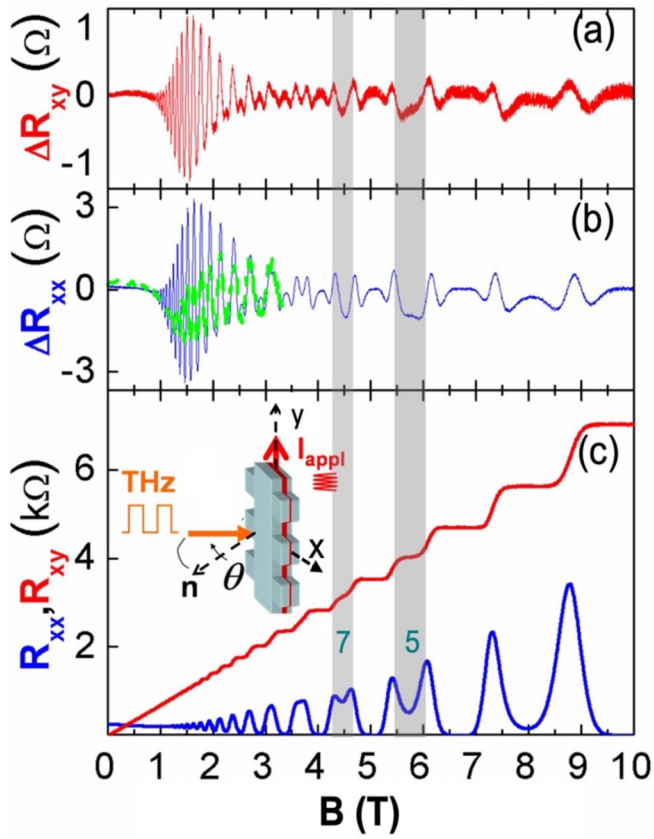

FIG. 2. Magnetotransport and photoinduced changes for **B** normal to the sample surface. (a) Change in the Hall resistance, ΔR_{xy}, induced by the THz radiation (3.15 meV). (b) Photoresponse, ΔR_{xx}, at $T = 4.2$ K (blue) and $T = 12$ K (green). (c) R_{xx} (blue) and R_{xy} (red) vs magnetic field ($I_{\text{appl}} \approx 3\,\mu$A rms). Filling factors $\nu = 5$ and 7 are indicated by the shaded vertical bars. Inset: Experimental sample configuration: the THz beam, collinear with the applied magnetic field, is shown by the horizontal (orange) arrow.

In these measurements the magnetic field was applied at angles of 38°–43° with respect to the normal to the sample surface to place the center of the filling factor $\nu = 7$ plateau at an applied field that makes the estimated Zeeman energy equal to the photon energy (3.15 meV) of one of the strongest and most stable THz lines of the Edinburgh Instruments FIRL100 optically pumped molecular gas laser. The mechanically chopped THz laser beam (linearly polarized with output power of ∼25 mW) was focused by an off-axis parabolic mirror onto the sample surface through the room-temperature and He-temperature windows of the cryostat. The THz beam propagation was parallel to the magnetic field, as shown schematically in the inset of Fig. 2(c). During most measurements, the sample was immersed in superfluid liquid helium. Absorption of the chopped beam induces a resistance change, $\Delta R_{xx} = R_{xx}$ (THz on)–R_{xx} (THz off), the photoresponse predominantly due to carrier heating of the 2DEG [34–38]. The ΔR_{xx} signal containing both current modulation and laser chopping frequencies was processed by a two lock-in amplifier arrangement and the signal at the chopping frequency (13 Hz) was demodulated and time averaged to produce the desired photoresponse signal.

III. RESULTS

Figure 2 shows the simultaneously measured resistances, R_{xx} and R_{xy} [Fig. 2(c)], and the corresponding photoresponse signals [Figs. 2(a) and 2(b)] are obtained with the double-modulation technique as a function of the applied field **B** for $\theta = 0$. At low temperature, the cyclotron-resonance absorption is observable only through its temperature modulation of the amplitude of the rapid Shubnikov–de Haas (SdH) oscillations in ΔR_{xx} (at these low fields). As a result, the position of the cyclotron-resonance absorption is obscured and the maximum in the modulated amplitude of the R_{xx} oscillations is shifted substantially to higher fields than the peak cyclotron-resonance absorption due to the exponential growth of the oscillation amplitude with B [39]. The cyclotron resonance becomes clearer at higher temperatures as the not fully developed minimum that can be seen in Fig. 2(b) at 12 K, because of the marked reduction in amplitude of the SdH oscillations. This minimum is still shifted to a higher field than the absorption maximum. The magnetotransmission measurements of the sample *in situ* at the same laser photon energy show the cyclotron-resonance transmission minimum at about 1 T. At higher fields and low temperature ($\leqslant$4.2), where the quantum oscillations are more widely separated and the quantum Hall plateaus appear in R_{xy}, the ΔR_{xx} signal shows a double-peak structure that is due to a temperature differential of the R_{xx} minima resulting from broad nonresonant absorption in the structure below the active InAs layer. In the following sections we concentrate on ΔR_{xx} at a series of tilt angles θ in the vicinity of the $\nu = 7$ QHE plateau in R_{xy} (and the corresponding R_{xx} minimum) determined by the normal component of the applied field, $B_\perp = B\cos\theta$. For $\theta = 0$ these features are shown by the shaded vertical bars in Fig. 2 for $\nu = 7$ and 5.

Figure 3(a) shows the B dependence of ΔR_{xx} at several tilt angles θ focusing on the field region immediately surrounding filling factor $\nu = 7$, which is determined by $B_\perp$. We attribute

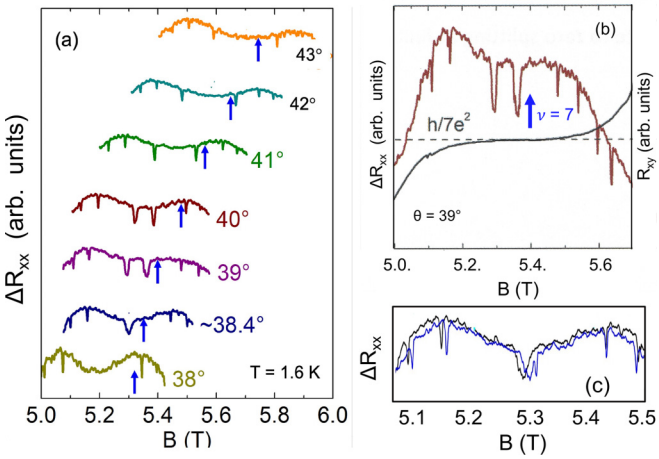

FIG. 3. (a) Angular dependence of ΔR_{xx} near $\nu = 7$ for I = 170 nA rms at $T = 1.6$ K. A single dip appears at $\theta_c = (38.4 \pm 0.4)^\circ$ at $B = 5.31$ T, splits with increasing θ, and *disappears* for $\theta < \theta_c$. Two pairs of satellite lines separated by larger applied fields are also visible. Vertical arrows show the calculated fields of incipience ($\nu = 7$) at each θ for $n_s = 7.1 \times 10^{11}$ cm^{-2}, obtained *in situ* in the Oxford magnet system from Shubnikov–de Haas measurements. (b) Comparison of the $\theta = 39^\circ$ photoresponse data with the corresponding R_{xy} data taken in the same experiment. (c) Field scan up (blue) and down (black) at 38.4° showing reproducibility and small hysteresis due to sweep rate and time constant.

the single feature at $B = 5.31$ T for $\theta_{7c} = 38.4^\circ$ to electron spin resonance of the 2DEG. Its field position is $B_{\rm ESR}$, which is found from $\hbar\omega_s = E_{\rm THz} = |g^*|\mu_{\rm B}B_{\rm ESR}$ and thus requires knowledge of g^* for electrons in the InAs quantum well at the Fermi energy. The single-particle conduction-band g factor of InAs is approximately–15, primarily due to its small energy gap and large spin orbit interaction. We describe in detail in the Appendix our estimate of g^* for electrons at the Fermi energy confined in a 15 nm quantum well from experimental "coincidence" measurements of low-field doubling of the Shubnikov–de Haas oscillation frequency [40,41] with modifications introduced to account for the angular dependence of electron-electron exchange and single-particle anisotropy introduced by confinement [42–46].

This estimate yields $|g^*| = 10.6$, in remarkably good agreement with the g factor obtained from the field position of the single broader dip in Fig. 3(a) at 38.4° ($|g^*| = 10.3$), which we have ascribed to electron spin resonance. Given the complexity of the calculation and assumptions, this excellent agreement is likely to be fortuitous. Nevertheless, it is consistent with our assignment and our use of $|g^*| = 10.3$ in the modeling shown in Fig. 6(a).

This single electron spin resonance feature *vanishes* for $\theta < \theta_{7c}$. We attribute this surprising result to two factors: (1) B is too small to achieve resonance in the edge channel for $B < B_{7\ell}$, [see Fig. 4(c)], and (2) for $B > B_{7\ell}$, when B is large enough to satisfy the electron spin resonance condition, the $\nu = 7$ edge channels are no longer formed; the chemical potential lies in nonconducting localized states associated with the $N = 3\uparrow$ Landau level in the latter case, and photoresponse from spin resonance is not detectable. We discuss this in more detail in Sec. V.

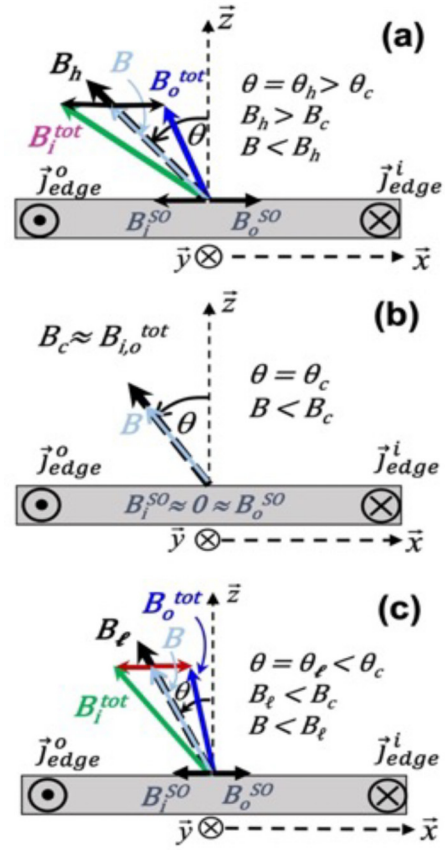

FIG. 4. Sample geometry and vector diagrams of the magnetic fields for $\nu \approx 7$. $\vec{j}^{\,i,o}_{\rm edge}$ (i, o, i.e., in, or out of the x-z plane along $\pm\hat{y}$) are current densities. **B** is rotated in the x-z plane by θ from the [001] (z direction) toward the $[\bar{1}\bar{1}0]$ crystalline axes. The spin orbit effective fields, $\mathbf{B}^{\rm SO}_{i,o}$, lie in the plane of the 2DEG perpendicular to the edge-channel currents. Panels (a–c) represent the low-field side of incipience with **B** (light blue arrow) $<$ $\mathbf{B}_h$, $\mathbf{B}_c$, and $\mathbf{B}_\ell$ (dashed black arrow), respectively. There are no edge channels for $\mathbf{B} > \mathbf{B}_h$, $\mathbf{B}_c$, or $\mathbf{B}_\ell$. Panel (b) shows the unique case for which $B^{\rm SO}_{\rm i,o} \approx 0$ and B_c also satisfies the spin-resonance condition.

For $\theta > \theta_{7c}$ the single line splits into two resonances that appear as individual dips, whose separation in B increases while the individual lines narrow with increasing θ. The average position of the two dips shifts up in applied field B, keeping $B_7\cos\theta \approx$ constant. Furthermore, there are two more widely separated doublets that can be seen at $\theta \approx \theta_{7c}$ and that only gradually shift in B with increasing θ. We attribute these "satellite" lines to EDSR from edge channels associated with the $\nu = 5$ and $\nu = 3$ plateaus, which are well below the Fermi energy in the 2D bulk (see Fig. 5). Such behavior has not been previously reported for GaAs [32–34] or Si [47]. We ascribe this unique behavior to strong spin orbit coupling that electrons experience in QHECs in InAs. The basic idea is related to that underlying the spin transistor [48], but in the present case the electrons are confined to incompressible quasi-1D QHECs with quantized conductance and suppressed backscattering, rather than the 2D electrons in the channel of the spin transistor. Our observations are consistent with EDSR transitions between pairs of spin-split incompressible quantum Hall edge channels, located at different positions

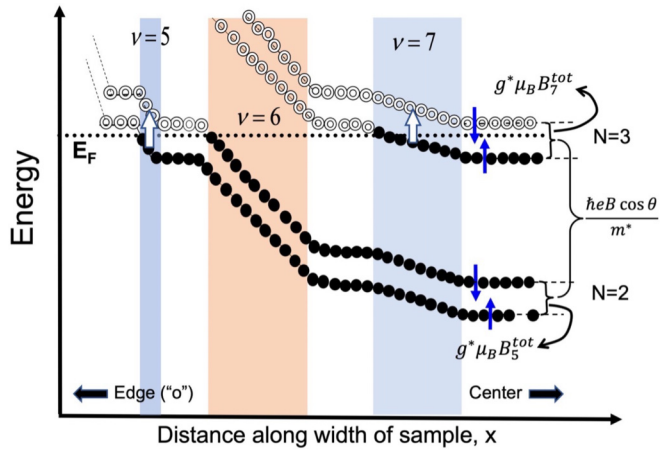

FIG. 5. Landau levels plotted vs x from the left edge (edge currents o) toward the center for $\theta = \theta_h > \theta_c$ and $\mathbf{B}_h > \mathbf{B}_c$ [see Fig. 3(a) for the corresponding vector diagram]. Solid black dots are occupied states and unfilled "donuts" are empty states. White arrows outlined in black represent EDSR transitions in the incompressible QHECs for $\nu = 5$ and 7. Shaded regions are incompressible strips; white backgrounds are compressible strips. The relative widths of the two types are not to scale; compressible strips are always larger than the incompressible strip that they surround. The incompressible strip for $\nu = 6$ corresponds to the cyclotron energy gap, whose driving voltage is $V_{\rm cyc} = \hbar(\omega_c - \omega_s)/e$.

relative to the edges of the sample, and the significant spin orbit fields associated with the electron momenta in channels that are not at, or very close to, incipience. At incipience the edge channels are located at the center and extend across the width of the Hall bar. The spin orbit effective fields add vectorially to the applied field for electron flow in edge channels along the $\pm y$ direction in the x-y plane as shown schematically in Fig. 4. In equilibrium the current flow along the y axis is equal in magnitude and opposite in direction for opposite edges, so one effective spin orbit field reduces the total magnetic field and the other increases it. For a particular filling factor ν this leads to two total fields ($\mathbf{B}^{\rm tot}_{\nu(i,o)}$), and thus possibly two applied fields for which the electron spin resonance condition can be satisfied, depending on the angle θ (see Fig. 4).

IV. THEORETICAL MODEL AND COMPARISON WITH EXPERIMENT

As mentioned above, the basic physics underlying our model and interpretation is based on the spin orbit effective field generated by the electrons in equilibrium currents of the topologically protected QHECs. This is combined with two constraints: (1) the total magnetic field satisfies the electron spin resonance condition; and (2) the normal component of the same field determines the edge-channel electronic properties, such as filling factor ν and location in the x direction relative to the sample edges (and thus their widths).

To understand the details, quantify the conditions, and justify our interpretation we begin by determining the total magnetic field for a particular filling factor ν, $\mathbf{B}^{\rm tot}_{\nu(i,o)}$, which is the vector sum of the applied magnetic field and the effective Rashba spin orbit fields, $\mathbf{B}^{\rm SO}_{\nu(i,o)}$; the subscripts denote the filling factor region, and the direction of current in the edge channel ("in" or "out") as shown in Fig. 4. In the edge channels these total fields determine the resonance condition, which is set by the effective g factor, g^*. As shown in Fig. 3, near the right edge of the sample (current in, subscript i) the applied and Rashba fields add to produce a total field that is *higher* (subscript h) than the applied field, and at the left edge (current out, subscript o) they add to produce a *lower* total field (subscript ℓ).

Figure 4(a) shows the basic geometry for a particular angle θ_{7h} that is larger than the unique angle θ_{7c}, and Figs. 4(b) and 4(c) show the situation for the unique angle θ_{7c} and for an angle $\theta_{7\ell}$ that is smaller than θ_{7c}, respectively. The persistent edge currents $j^{i,o}_{\rm edge}$ flow along the $\pm y$ directions that correspond to {110} crystalline axes, independent of θ. As the axis of the structural asymmetry lies along the growth direction z ([001]), the effective spin orbit magnetic fields, of magnitude $B^{\rm SO}_{\nu(i,o)} = \frac{2\alpha_R k}{g^*\mu_B B}$, lie in the x-y plane along $\pm x$, perpendicular to the edge currents along $\pm y$. The latter are the directions of the wave vector $\mathbf{k} = m^*\mathbf{v}/\hbar.$, where $\mathbf{v}$ is the electron velocity vector and m^* its effective mass. The resulting magnitude of the total magnetic field can be written

$$B^{\rm tot}_{\nu(i,o)}(\theta) = \pm\sqrt{B^2\cos^2\theta + \left(B\sin^2\theta \pm B^{\rm SO}_{\nu(i,o)}\right)^2}, \qquad (1)$$

where the sign is determined by the direction of current flow (+ for i and – for o). Thus for a particular angle θ, the two total fields that can satisfy the spin-resonance condition are given by the solutions to $\hbar\omega_s = \omega_{\rm THz} = g^*\mu_B B^{\rm tot}_{\nu(i,o)}$ where $B^{\rm tot}_{\nu(i,o)}$ is a function of B, $B^{\rm SO}_{\nu(i,o)}$, and θ.We note that the lower applied field at which this condition is satisfied corresponds to the right edge channel in Fig. 3 (subscript i), while the current in the left edge channel (subscript o) satisfies the condition at higher applied field (closer to incipience). Both fields must be lower than the corresponding incipience field, so that $B\cos\theta$ leads to a chemical potential (E_F at $T = 0$, in Fig. 4) that does not lie in states associated with the 3↑ Landau level, i.e., $\nu < 7$, where edge channels in the ideal case cease to exist.

We assert that the central resonance feature at $\theta = \theta_{7c}$ is directly connected to the incipient formation of the $\nu = 7$ incompressible QHECs. As indicated in Fig. 5, "incipience" takes place at applied magnetic fields $\mathbf{B}$ corresponding to the electrochemical potential in the gap between the R_{xx} conductance peaks for the $N = 3\uparrow$ and $N = 3\downarrow$ Landau levels (i.e., the $\nu = 7$ R_{xy} plateau) at a field close to that corresponding to complete filling of the $N = 3\uparrow$ Landau-level states, where N is the Landau quantum number (see Sec. V, Discussion). The current in each incompressible edge channel is $I = \frac{e^2}{h}V$, where h is Planck's constant, e is the magnitude of the charge of the electron, and V is the voltage drop across the channel, independent of filling factor ν. However, the width w_ν of the incompressible edge channel with an integer value of ν, which separates two compressible regions, does depend on ν through the local electron density profile, $n_s(x)$, along the x direction in the vicinity of the edge channel, as discussed below.

The current in the incompressible spin-split edge channel can be written as

$$I_\nu = \frac{e^2}{h}\left(\frac{\hbar\omega_s}{e}\right) = e\eta w_\nu \mathrm{v}, \qquad (2)$$

where $\eta = \frac{1}{2\pi l_B^2} = \frac{e}{h} B\cos\theta$ is the Landau-level degeneracy with l_B the radius of the quantum cyclotron orbit (magnetic length). The magnitude of the effective spin orbit field is given in terms of the width w_ν by

$$B^{\rm SO}_{\nu(i,o)} = \frac{2}{\cos\theta}\frac{\alpha_R m^*}{\hbar e w_\nu}, \tag{3}$$

where $w_\nu(x)$ depends on the location of the edge channel in the x direction.

In equilibrium for a magnetic field along the z direction the location of the edge channels along x is determined by the intersection of the chemical potential in the 2D bulk (and the compressible strips) with the electron density distribution, $n_s(x)$. For our model we employ the simple expression for $n_s(x)$ derived by Chklovskii *et al.* [17], $n_s(x)/n_s = \sqrt{x/(2l+x)}$, where n_s is the bulk 2D value of the electron density and $2l$ is the nonlinear screening length, to calculate the approximate locations (and the corresponding widths) of the various edge channels. We note that the actual [three-dimensional (3D)] sample geometry is complicated, as are the corresponding electrostatics. The band bending and the large electron density in the well in the absence of intentional doping is determined by the surface or interface pinning of the electrochemical potential and the effects of etching and deep-level defects. There has been discussion for many years about the origin of the electrons populating InAs quantum wells in this heterostructure system; see, e.g., [49]. Dealing with these complexities is beyond the scope of the present work, and for our purposes the Chklovskii expression is both simple and, we believe, adequate.

For incompressible strips associated with integer ν, the width is given by $w_\nu^2 \approx \kappa\hbar\omega_s/[e^2|dn_s(x)/dx|_{x=x_\nu}]$. Here, κ is the low-frequency dielectric constant, x_ν is the position of the νth incompressible strip, and $n_s(x_\nu) = \nu\eta$. That is, for a given ν the locations of the edge channels are determined by the positions in x of the intersections of $n_s = \nu\eta$, with $n_s(x)$ vs x, where the Landau-level degeneracy η is determined by $B_\perp$. The locations of the edge channels can be obtained from

$$\frac{n_s(x_\nu)}{n_s} = \sqrt{\frac{x_\nu}{(2l+x_\nu)}} = \frac{B\cos\theta}{B_\nu\cos\theta_\nu}, \tag{4}$$

where n_s is the bulk 2D electron density in the absence of depletion.

For small variations in θ and B about θ_ν and B_ν we find from Eq. (4) the following expressions for the channel location x_ν, and the derivative of the spatial variation of the density $[dn(x)/dx]_{x=x_\nu}$,

$$x_\nu \approx \frac{l}{\tan\theta_\nu(\theta-\theta_\nu) - \frac{B-B_\nu}{B_\nu}}, \tag{5}$$

and

$$\frac{dn_s(x)}{dx}|_{x=x_\nu} \approx \frac{n_s}{l}\left[\tan\theta_\nu(\theta-\theta_\nu) - \frac{B-B_\nu}{B_\nu}\right]^2. \tag{6}$$

The variables θ and B are not independent, but for small changes Eqs. (5) and (6) should be adequate for our purposes. We use Eqs. (5) and (6) in conjunction with Eq. (3) to obtain the spin orbit field in terms of the spatial derivative of the density profile,

$$B^{\rm SO}_\nu = \frac{2\alpha_R m^*}{\hbar\sqrt{\kappa\hbar\omega_s}\cos\theta_\nu}\sqrt{\frac{dn_s(x)}{dx}|_{x=x_\nu}} \tag{7}$$

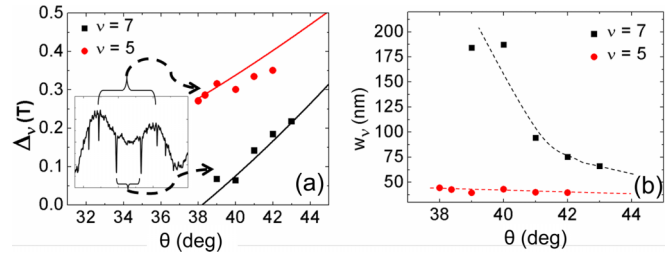

FIG. 6. (a) Splitting of the spin-resonance dips deduced from the photoresponse data (black squares and red dots) as indicated in the inset. The solid lines are calculations of the splittings for $\nu = 7$ and 5 with $m^* = 0.042\,m$, $g^* = -10.3$, $\alpha_R = 1.1\times10^{-9}$ eV cm, and $n_s = 7.05\times10^{11}$ cm^{-2}. (b) Widths w_ν of the QHECs vs tilt angle θ calculated from Eq. (3) and the experimentally measured splittings; the dashed lines are guides to the eye.

At incipience the width of the channels is approximately the sample width, 250 μm. From Eq. (3) this yields a spin orbit field of about 0.05 mT, which is negligible compared to the applied field, so at incipience for $\theta = \theta_{7c} = 38.4^\circ$, $B^{\rm tot}_{7(i,o)} \approx B_{7c} = B_{\rm ESR}$. Thus a single-resonance feature is observed from two very wide overlapping channels, broadened by disorder.

We focus now on the $\theta - B$ region close to this unique angle θ_{7c}. For θ and B close to such special points in the parameter space, we can write $B_{\rm ESR} \approx B^{\rm tot}_{\nu(i,o)} = B \pm B^{\rm SO}_\nu \sin\theta_\nu$ and thus

$$(B - B_\nu) \pm B^{\rm SO}_\nu \sin\theta_\nu = 0. \tag{8}$$

Substituting for $B^{\rm SO}_\nu$ from Eq. (7) we have

$$\pm(B - B_\nu) = \Lambda_\nu |B_\nu \tan\theta_\nu(\theta-\theta_\nu) - (B - B_\nu)|, \tag{9}$$

where the dimensionless parameter $\Lambda_\nu = \frac{\nu\sin\theta_\nu}{\pi l_{\rm SO}}\sqrt{\frac{e^2}{\kappa n_s l\hbar\omega_s}} > 0$ and the spin orbit length $l_{\rm SO} = \frac{\hbar^2}{m^*\alpha_R}$. Finally, by combining these results for fields and angles close to the special point (B_{7c}, θ_{7c} in the present case) we find for the angular dependence,

$$B^{\rm SO}_\nu(\theta) \approx \frac{\Lambda_\nu}{1+\Lambda_\nu}\frac{B_\nu}{\cos\theta_\nu}(\theta - \theta_\nu). \tag{10}$$

Equation (10) allows us to relate the spin orbit field of the edge channel to the tilt angle θ relative to the unique incipience angle θ_{7c} and to determine the approximate magnetic-field splitting over small ranges of fields (~0.5 T) and angles (5°) relative to this special point.

Figure 6(a) shows the magnetic-field separation of the central feature and the next pair of resonances (the first pair of satellite lines, as shown in the inset) as a function of θ. This splitting is $\Delta_\nu \equiv |\mathbf{B}^{\rm tot}_{\nu i} - \mathbf{B}^{\rm tot}_{\nu o}| \approx 2\sin\theta B^{\rm SO}_\nu$, which implies a symmetry between the solutions for $B^{\rm SO}_{\nu i}$ and $B^{\rm SO}_{\nu o}$, namely, $B^{\rm SO}_{\nu i} = -B^{\rm SO}_{\nu o}$. The experimental results do not exhibit such a simple symmetric relationship for the spin orbit fields, which are always opposite in direction, but not equal in magnitude, especially for the larger angles. The resonance for $B^{\rm SO}_{\nu o}$ occurs

at a smaller decrease in field from B_h than that for B_{vi}^{SO}, so the corresponding edge channel is wider and $|B_{vo}^{SO}| < |B_{vi}^{SO}|$. Nevertheless, the contributions from the two edge channels add to produce the total splitting and the sum is not significantly different from the simple expression. For a representative set of parameters the simple relationship yields numerical values that are remarkably close to our experimental observations as seen in Fig. 6(a).

We can also identify the first satellite pair of lines (the next more widely separated dips in R_{xx}) as electron spin resonance for incompressible QHECs with $\nu = 5$ and estimate the corresponding magnetic-field splittings (given in the figure). From this model and the experimentally determined splittings Δ_ν, we extract an estimate of the widths of the respective QHECs at several values of θ, as shown in Fig. 6(b). The widths of the $\nu = 7$ QHECs decrease significantly with increasing θ as they move from the sample center toward the edges, as expected. The depletion potential $V(x)$ and electron density $n_s(x)$ change much more rapidly close to the edges, and consequently the QHEC width decreases very rapidly in that region, as it is inversely proportional to the rate of decrease of $n_s(x)$. The $\nu = 5$ channel is little affected by changing θ as the Landau levels associated with it lie energetically well below the Fermi level in the 2D bulk and thus the corresponding pair of Landau levels, $2\uparrow$ and $2\downarrow$, are much closer to the edges at the Fermi energy (see Fig. 5). Theoretically, the ideal width of an incompressible QHEC is given by $w_\nu = \sqrt{2\nu + 1} l_B$ [50]. These widths are in reasonable agreement with our experimental results, e.g., on the $\nu = 7$ plateau, where $B_\perp \sim 4.2$ T, $l_B = 12.6$ nm, and this gives $w_7 \approx 49$ nm and $w_5 = 42$ nm. The values extracted from our splitting measurements and Eq. (3) in the vicinity of $\nu = 7$ lie in the range 60–180 nm, and for $\nu = 5$ the values are about 30–40 nm.

The disappearance of the central feature for $\theta = 38^\circ < \theta_{7c}$ remains to be explained in detail, and there are several subtleties associated with the calculation and the location of the EDSR lines that require further attention and explanation. We address these issues in the following section.

V. DISCUSSION

Aspects of the experimental results show remarkably good agreement with the model described in the previous section for $\nu = 7$ and 5, e.g., the existence of multiple lines, the magnitudes of the field separations between pairs of lines, the tilt-angle dependence of these splittings, and the single line at θ_c. However, there are issues that we have not addressed in detail, the most striking of which is the disappearance of the spin resonance in the photoresponse for tilt angles less than θ_c, as can be seen in Fig. 3(a) (N.B. the strong pair of dips is associated with the $\nu = 5$ plateau).

For several years a group at the Max-Planck Institute in Stuttgart has studied the microscopic behavior of the Hall voltage and current distributions across the width of samples under quantum Hall effect conditions. Their extensive experimental (scanning probe) investigations at the nanoscale combined with theoretical calculations have led to considerably improved understanding of the edge channels and the detailed behavior of the currents and Hall potentials, and have helped us unravel some of the subtleties of our experimental results (see, e.g., [20,23–26]). We summarize here results and conclusions that are pertinent to our work: (1) On the plateaus of R_{xy} vs $B\cos\theta$ in the vicinity of $\nu =$ int. (integer) there exists a region of $\nu <$ int. (higher fields), over which the electrical properties are dominated by *2D-bulk behavior* and edge channels are *not* formed. (2) There is disorder of compressible and incompressible regions in the vicinity of $B_{\nu=\text{int.}}$, for a range of magnetic fields both below and above. (3) For lower fields on the plateau, where $\nu >$ int., edge channels (incompressible strips) are formed and dominate the electrical behavior. (4) For larger ν plateaus the field $B_{\nu=int.}$ is higher than the field corresponding to the apparent center of the respective plateau (or the center of the corresponding minimum of R_{xx}).

To aid further discussion we refer to Fig. 5, which is a sketch for the left edge of the energies of the Landau-level spin pairs ($3\uparrow$, $\downarrow$ and $2\uparrow$, $\downarrow$) showing the corresponding edge channels (incompressible strips), the level occupancy, and the location of EDSR transitions vs lateral position x for the $\nu = 7$ edge channels close to incipience. The Fermi energy lies energetically in the Zeeman gap between $3\uparrow$ and $3\downarrow$, such that all states associated with Landau-level $3\uparrow$ are filled, so edge-channel formation is expected. The incompressible strips for the $\nu = 7$ and 5 edge channels are shown as vertical shaded regions, with the strip for $\nu = 5$ much narrower than that for $\nu = 7$ because of the more rapid change of $n_s(x)$ closer to the edge. The incompressible strip for the $\nu = 6$ plateau is also shown by a shaded region. The even-integer incompressible strips are wider for a given x position because of the larger energy separation between the $3\downarrow$ and $2\uparrow$ Landau levels (about 3.3 $\hbar\omega_s$), and the correspondingly larger driving voltage, $V_{\text{cyc}} = \hbar(\omega_c - \omega_s)/e$. In the following paragraphs, in which we discuss the details of various aspects of the interpretation, all discussion refers to the $\nu = 7$ region of fields and angles; therefore, in the interest of simplifying a complex notation, we drop the ν subscript for the remainder of this section.

The configuration of magnetic fields that corresponds to the single broader dip in the photoresponse at $\theta = 38.4^\circ = \theta_c$ is shown in Fig. 4(b). In this case, as discussed above, the incompressible strips are located close to the center of the sample in the x direction and the spin orbit fields are negligible compared to the incipience field; thus the two *total fields* have the same magnitude, B_c, and this is equal to B_{ESR}, the field that satisfies the spin-resonance condition.

For the THz photon energy of 3.15 meV (25.4 cm^{-1}) the *only* θ and B that can satisfy both the incipience condition and the resonance condition simultaneously are $\theta_c = 38.4^\circ$ and $\mathbf{B}_c \approx 5.3$ T. We note that there is disorder in this region (point 2 above) that may affect the exact position of incipience and that also contributes to broadening of the EDSR resonance(s). The pairs of narrower resonant dips that are observed at larger tilt angles at significant field separations from the incipience field correspond to edge channels that are well formed, narrower, and less susceptible to disorder because of their topological protection.

We turn now to more detailed discussion of smaller tilt angles $\theta_\ell < \theta_c$ [see Fig. 4(c)], which correspond to the *disappearance* of the central single dip associated with $\nu = 7$. The incipience field B_ℓ, determined by $B_\ell\cos\theta_\ell$, that corresponds to the condition for exact filling of seven Landau

levels, is smaller than B_c; thus it is too small to excite spin resonance, $B_\ell < B_{\rm ESR}$. However, as mentioned previously, for fields greater than the corresponding incipience field, edge channels are *not* formed. Edge-channel formation requires maintaining full population of the 3↑ Landau level, and this requires $B < B_\ell < B_c$. However, as can be seen from Fig. 4(c) (and is verified by calculation), decreasing B at constant θ cannot yield a total field greater than B_ℓ; i.e., the increase of $B_o^{\rm SO}$ can never overcome the decrease of B required to produce it. As a result, $B_{\rm ESR}$ cannot be reached and edge-channel spin resonance is not possible for the edge current out (o) of the plane in Fig. 4(c). Therefore spin resonance can only occur in this case via exciting transitions from compressible states (the bulk 2D states and the compressible strips), but these (localized) states do not contribute to electrical conductivity. The photoresponse is sensitive only to changes in the conductivity of the edge channels under the resonant absorption of photons from the THz laser. We conclude that for $\theta < \theta_c$, spin-resonance transitions are not observable in our photoresponse measurements, consistent with its initially puzzling disappearance in the experiments for $\theta < \theta_c$.

This discussion has implications for $\theta = \theta_h > \theta_c$, as well. Incipience is achieved under these conditions at larger applied magnetic fields, $B_h > B_c$, as shown schematically in Fig. 4(a). We note that the calculated incipience field B_h for which the 3↑ Landau level is completely occupied is shifted to higher fields than the center of the broad ΔR_{xx} minima for most angles. The upright arrows in Figs. 3(a) and 3(b) indicate the expected positions of the incipience fields at each θ based on an electron density, $n_s = 7.1 \times 10^{11}\,{\rm cm}^{-2}$, determined from the low-field Shubnikov–de Haas oscillation frequency. These fields are higher than the centers of the broad background minima in ΔR_{xx}, which appear approximately at the centers of the corresponding R_{xy} plateaus. Figure 3(b), which compares directly the ΔR_{xx} EDSR spectrum with the R_{xy} plateau for $\theta = 39^\circ$, clearly shows both EDSR dips below the center of the plateau and the field corresponding to $\nu = 7$. These results are consistent with the scanning probe results on GaAs/(AlGa)As heterostructures discussed previously. As edge channels are formed only for fields *less* than the incipience field, the higher-field dip of the central pair at 43° would appear to be excluded, as it lies about 75 mT higher than the incipience field (a difference of 55 mT in $B_\perp$). It is possible, however, that at and near incipience, due to disorder and lateral inhomogeneities with islands of compressible electron liquid embedded in an incompressible electron sea, the applied field at incipience is shifted even higher than we calculated. Also, these inhomogeneities could lead to different regions of incompressible electrons forming distinct topologically protected channels at slightly different fields. Thus a combination of disorder and experimental and calculational uncertainties could account for the observed behavior. We are more confident of the estimated incipience fields for angles close to θ_c because the angle and field for this singular case are clearly marked by the single EDSR dip (within error caused by disorder), and the spin orbit field is negligible.

For $B < B_h$ the conditions for observation of spin resonance can be achieved in both edge channels. The right edge channel with current into the page (i) adds its effective spin orbit field to the applied field to produce a larger total field, as shown in Fig. 3(a). If B is close to B_h, the total field can be ≈0.4 T higher than $B_c = B_{\rm ESR}$; in this case B must be reduced enough that $B_i^{\rm tot} \approx B + B_i^{\rm SO}\sin\theta = B_{\rm ESR}$, overcoming the increase of $B_i^{\rm SO}$ that opposes the decrease of B. On the other hand, the left edge channel produces a spin orbit field $\mathbf{B}_o^{\rm SO}$ that is oppositely directed and therefore subtracts from the applied field to produce a *smaller* total field, $B_o^{\rm tot} \approx B - B_o^{\rm SO}\sin\theta$, that can be tuned to $B_{\rm ESR}$ with a much smaller reduction in B. Thus there are two applied fields that for two distinct values of $B < B_h$ give a total field equal to $B_{\rm ESR}$, one for each edge channel on opposite sides of the sample with a difference in the contributions from $B_i^{\rm SO}$ compared with that of $B_0^{\rm SO}$. This difference in applied field for the two different current directions needed to achieve $B^{\rm tot} = B_{\rm ESR}$ is much smaller for angles close to θ_c. There is also an asymmetry between the two channels introduced by the applied current (see, e.g., [25,26]) that may contribute to the observed behavior, and which we have not included in our analysis.

VI. SUMMARY AND CONCLUSIONS

In summary we have probed effects of Rashba-type spin orbit interaction of quasi-2D electrons confined in an InAs quantum well in incompressible quantum Hall edge channels through sensitive photoresponse detection of electric-dipole spin-resonance transitions under THz laser excitation. Multiple sharp lines, whose positions depend on the tilt angle of the applied magnetic field with respect to the normal to the plane of the two-dimensional electron gas, appear as sharp dips in the photoresponse. A single central line appears at a unique angle θ_c and splits into two lines whose magnetic-field separation increases with increasing θ, but which disappears abruptly for $\theta < \theta_c$. We have developed a simple model of this unusual behavior in the magnetic-field region expected for electron spin resonance. Our model is based on the equilibrium edge-channel electrostatics picture [17,18] of the quantum Hall effect combined with the oppositely directed spin orbit magnetic fields generated by the equilibrium currents in odd filling factor QHECs adding vectorially to the applied field. The total field thus produced can be tuned to satisfy the condition for THz EDSR for multiple applied fields, usually two distinct values of $\mathbf{B}$ for each odd-integer edge channel. For $\nu = 7$ these channels are incipient and very broad near the center of the sample width and move toward opposite edges while narrowing as the field is decreased. For applied field $\mathbf{B}$ greater than the incipience field there are no edge channels formed and no corresponding EDSR is observed. This model yields semiquantitative agreement with the experimental results, and we believe that remaining uncertainties are not large enough to affect our conclusions.

Similar effects should be observable in materials with small spin orbit coupling such as GaAs or graphene, but with much smaller splittings. For GaAs 2DEGs the splitting of the central ESR feature should be roughly 1/5 of that seen in our samples for a SO coupling parameter $\alpha_R = 2 \times 10^{-12}$eV m and $l = 200$ nm [17]). In the absence of exchange enhancement, $g^* = -0.44$ for GaAs, and this yields a very small spin splitting energy, which could make these edge-channel effects difficult to observe. Most importantly, the splitting behavior is only observable for magnetic fields oriented at significant

angles θ to the normal to the sample surface. At normal incidence ($\theta = 0$) the two total magnetic fields in Eq. (1) are equal in magnitude and thus yield a single resonance.

ACKNOWLEDGMENTS

We are grateful to Emmanuel Rashba for his collaboration in this work. One of us, B.D.M., is especially indebted to Prof. Rashba for his continuing contact spanning more than 50 years. A.V.S. and B.D.M. thank L. Freund for a helpful discussion and private communication. This work was supported in part by the Defense Advanced Research Projects Agency (DARPA) SPINS Program through the Office of Naval Research (ONR) Grant No. N000140010591, by the National Science Foundation (NSF), Materials World Network Award No. 1008138, and by internal funds from the office of the Provost at the University at buffalo.

APPENDIX: g-FACTOR DETERMINATION

The magnitude of the single-particle effective g factor of InAs at the bottom of the conduction band (–14.6) is much larger than that of, e.g., GaAs (–0.44), primarily because of the much smaller energy gap of InAs (0.42 eV) relative to GaAs (1.52 eV) (see [51] for relevant band parameters of these materials). The smaller gap and stronger coupling of the p-like and s-like bands at the Brillouin-zone center of InAs lead to greater mixing of the spin orbit interaction of the p-like states into the s-like conduction-band states and an increased magnitude of the g factor. The stronger coupling of the bands in InAs also leads to considerably larger nonparabolicity than is found in GaAs. Consequently, we expect a substantially decreased magnitude of the single-particle effective g factor and a correspondingly larger effective mass (the bottom of the band effective mass of InAs $m^* = 0.026\,m$) for electrons whose energy is the quantum-well confinement energy plus Fermi energy higher than the bottom of the bulk energy band.

To obtain an effective g factor to use in the calculations of the splittings for comparison with experimental observations, we made an initial estimate of $|g^*|$ from measurements of low-field Shubnikov–de Haas oscillations and the simple coincidence expression for Shubnikov–de Haas oscillation frequency doubling [40,41]. This approach yields $|g^*|(m^*/m) = \cos\theta_d = 0.375 \pm 0.005$ at $\theta_d = 68^\circ$ for an electron density $n_s = 10^{12}\,\mathrm{cm}^{-2}$ measured in the same experiment. Here θ_d is the doubling angle. With an effective mass $m^*/m = 0.042$ from cyclotron resonance measurements in a separate magnet system at a photon energy of 10.4 meV and $n_s \sim 10^{12}\,\mathrm{cm}^{-2}$ we find $|g^*| = 8.9$. With $m^*/m = 0.038$ from *in situ* cyclotron resonance measurements at a photon energy of 3.15 meV and a lower electron density, $n_s = 7.1 \times 10^{11}\,\mathrm{cm}^{-2}$, $|g^*| = 9.9$.

However, these simple estimates ignore many-electron exchange effects and single-particle anisotropy due to confinement, both of which decrease the measured g factor with tilt angle θ. Following Ref. [42], we account for exchange effects by first calculating the exchange contribution to the spin splitting in the limit of large Landau quantum numbers [43] and then using the modified coincidence expression given in [44] to incorporate both a g factor contribution from exchange ($\propto \cos\theta$) and an anisotropic single-particle g factor [45,46]. From $E_{\mathrm{ex}} = \alpha\hbar\omega_c$ and $\alpha = \frac{\ln(2k_F a_B)}{\pi k_F a_B}$, where k_F is the Fermi wave vector, and a_B is the effective Bohr radius, we obtain (for $n_s = 1 \times 10^{12}\,\mathrm{cm}^{-2}$ and $m^* = 0.042\,m$) $|g_{\mathrm{ex}}^{\mathrm{th}}| = 7.1$. We use this theoretical exchange contribution in the modified coincidence expression and find $|g_{\mathrm{sp}}(\theta_d)| = [\frac{1}{m^*/m} - |g_{\mathrm{ex}}^{\mathrm{th}}|]\cos\theta_d$, where θ_d is the angle at which the Shubnikov–de Haas oscillation frequency doubles and $g_{\mathrm{sp}}(\theta)$ is the anisotropic single-particle g factor. In the region of coincidence Landau quantum numbers are > 10, and use of the semiclassical model, for which a constant exchange g factor can be defined, is reasonable. We define total g values, $g_{||} = g_{||,\mathrm{sp}} + g_{\mathrm{ex}}$, and $g(\theta) = g_{\mathrm{sp}}(\theta) + g_{\mathrm{ex}}\cos\theta$, and use results of Ref. [42] for the ratio $\frac{g_{||,\mathrm{sp}}}{g_{\perp,\mathrm{sp}}} = 1.6$, where $g_{||,\mathrm{sp}}$ and $g_{\perp,\mathrm{sp}}$ are the single-particle g factors parallel and perpendicular to the quantization axis, respectively. As this result was obtained for an InAs structure with a narrow quantum well (3.5 nm) and different barrier material, it can be considered only semiquantitative when applied to the present sample. Assuming a cylindrically symmetric g tensor $g_{sp}(\theta) = [g_{||,\mathrm{sp}}^2\cos^2\theta + g_{\perp,\mathrm{sp}}^2\sin^2\theta]^{1/2}$ and this ratio, we determine $g_{||,\mathrm{sp}}$ and $g_{\perp,\,\mathrm{sp}}$ for our sample from the coincidence condition at $\theta_d = 68^\circ$. The results are as follows: $|g_{\mathrm{sp}}(68^\circ)| = 5.5$, $|g_{||,\mathrm{sp}}| = 7.4$, and $|g_{\perp,\,\mathrm{sp}}| = 4.6$. Using these numbers we calculate the single-particle g factor and the total effective g factor at $\theta = 40^\circ$, the region of our experiments. We find $|g_{\mathrm{sp}}(40^\circ)| = 6.4$ and, finally, $|g^*(40^\circ)| = |g_{\mathrm{sp}}(40^\circ)| + |g_{\mathrm{ex}}^{\mathrm{th}}|\cos 40^\circ = 10.6$. This result is in remarkably good agreement with the value of g^* obtained from the location of the single-resonance dip shown in Fig. 3(a), especially in view of the various approximations and assumptions involved in the analysis. Although the excellence of the agreement may be serendipitous, it supports our choice of $|g^*| = 10.3$ as reasonable for the calculation shown in Fig. 6.

[1] K. v. Klitzing, G. Dorda, and M. Pepper, New Method for High-Accuracy Determination of the Fine-Structure Constant Based on Quantized Hall Resistance, Phys. Rev. Lett. **45**, 494 (1980).

[2] D. J. Thouless, M. Kohmoto, M. P. Nightingale, and M. den Nijs, Quantized Hall Conductance in a Two-Dimensional Periodic Potential, Phys. Rev. Lett. **49**, 405 (1982).

[3] Q. Niu, D. J. Thouless, and Y.-S. Wu, Quantized Hall Conductance as a topological invariant, Phys. Rev. B **31**, 3372 (1985).

[4] B. A. Bernevig, T. L. Hughes, and S.-C. Zhang, Quantum spin Hall effect and topological phase transition in HgTe quantum wells, Science **314**, 1757 (2006).

[5] M. König, S. Wiedmann, C. Brüne, A. Roth, H. Buhmann, L. W. Molenkamp, X. L. Qi, and S-C. Zhang, Quantum spin Hall insulator state in HgTe quantum wells, Science **318**, 766 (2007).

[6] C. L. Kane and E. J. Mele, Quantum Spin Hall Effect in Graphene, Phys. Rev. Lett. **95**, 226801 (2005); Z_2 Topological Order and the Quantum Spin Hall Effect, **95**, 146802 (2005).

[7] B. A. Bernevig and S.-C. Zhang, Quantum Spin Hall Effect, Phys. Rev. Lett. **96**, 106802 (2006).

[8] Semiconductor Spintronics and Quantum Computation, *Nanoscience and Technology*, edited by D. D. Awschalom, D. Loss, and N. Samarth (Springer, Berlin, 2002).

[9] I. Zutic, J. Fabian, and S. Das Sarma, Spintronics: Fundamentals and applications, Rev. Mod. Phys. **76**, 323 (2004).

[10] D. D. Awschalom and N. Samarth, Spintronics without magnetism, Physics **2**, 50 (2009).

[11] N. Gisin and R. Thew, Quantum communication, Nat. Photonics **1**, 165 (2007).

[12] A. Manchon, H. C. Koo, J. Nitta, S. M. Frolov, and R. A. Duine, New perspectives for Rashba spin-orbit coupling, Nat. Mater. **14**, 871 (2015).

[13] E. I. Rashba and Al. L. Efros, Efficient electron spin manipulation in a quantum well by an in-plane electric field, Appl. Phys. Lett. **83**, 5295 (2003).

[14] E. I. Rashba and Al. L. Efros, Orbital Mechanisms of Electron-Spin Manipulation by an Electric Field, Phys. Rev. Lett. **91**, 126405 (2003).

[15] E. I. Rashba and V. I. Sheka, Electric dipole spin resonances, in *Modern Problems in Condensed Matter Sciences*, Landau Level Spectroscopy, Vol. 27, edited by G. Landwehr and E. I. Rashba (Elsevier, Amsterdam, 1991), pp. 131–206.

[16] B. I. Halperin, Quantized Hall conductance, current-carrying edge states, and the existence of extended states in a two-dimensional disordered potential, Phys. Rev. B **25**, 2185 (1982).

[17] D. B. Chklovskii, B. I. Shklovskii, and L. I. Glazman, Electrostatics of edge channels, Phys. Rev. B **46**, 4026 (1992).

[18] D. B. Chklovskii, K. A. Matveev, and B. I. Shklovskii, Ballistic conductance of interacting electrons in the quantum Hall regime, Phys. Rev. B **47**, 12605 (1993).

[19] M. Büttiker, Absence of backscattering in the quantum Hall effect in multiprobe conductors, Phys. Rev. B **38**, 9375 (1988).

[20] E. Ahlswede, P. Weitz, J. Weis, K. von Klitzing, and K. Eberl, Hall potential profiles in the quantum Hall regime measured by a scanning force microscope, Phys. B (Amsterdam) **298**, 562 (2001).

[21] A. Uri, Y. Kim, K. Bagani, C. K. Lewandowski, S. Grover, N. Auerbach, E. O. Lachman, Y. Myasoedov, T. Taniguchi, K. Watanabe *et al.*, Nanoscale imaging of equilibrium quantum Hall edge currents and of the magnetic monopole response in graphene, Nat. Phys. **16**, 164 (2020).

[22] K. C. Nowack, E. M. Spanton, M. Baenninger, M. König, J. R. Kirtley, B. Kalisky, C. Ames, P. Leubner, C. Brüne, H. Buhmann *et al.* Imaging currents in HgTe quantum wells in the quantum spin Hall regime, Nat. Mater. **12**, 787 (2013).

[23] K. Panos, R. R. Gerhardts, J. Weis, and K. von Klitzing, Current distribution and Hall potential landscape towards breakdown of the quantum Hall effect: A scanning force microscopy investigation, New J. Phys. **16**, 113071 (2014).

[24] K. von Klitzing, R. Gerhardts, and J. Weis, 25 jahre quanten-Hall-effekt, Phys. J. **4**, 37 (2005).

[25] P. Haremski, M. Mausser, A. Gauss, K. von Klitzing, and J. Weis, Electrically induced breakdown of the quantum Hall effect at different Hall bar widths: Visualizing the edge- and bulk-dominated regimes within a quantum Hall plateau, Phys. Rev. B **102**, 205306 (2020).

[26] R. R. Gerhardts, K. Panos, and J. Weis, Current-induced asymmetries of incompressible strips in narrow quantum Hall systems, New J. Phys. **15**, 073034 (2013).

[27] S. Kim, J. Schwenk, D. Walkup, Y. Zeng, F. Ghahari, S. T. Le, M. R. Slot, J. Berwanger, S. R. Blakenship, K. Watanabe, T. Taniguchi, F. J. Giessibl, N. B. Zhitenev, C. R. Dean, and J. A. Stroscio, Edge channels of broken-symmetry quantum Hall states in graphene visualized by atomic force microscopy, Nat. Commun. **12**, 2852 (2021).

[28] J. Nitta, T. Akazaki, H. Takayanagi, and T. Enoki, Gate Control of Spin-Orbit Interaction in an Inverted $In_{0.53}Ga_{0.47}As/In_{0.52}Al_{0.48}As$ Heterostructure, Phys. Rev. Lett. **78**, 1335 (1997).

[29] R. Winkler, *Spin Orbit Coupling Effects in Two-Dimensional Electron and Hole Systems* (Springer Verlag, Berlin, 2003).

[30] Yu. A. Bychkov and E. I. Rashba, Oscillatory effects and the magnetic susceptibility of carriers in inversion layers, J. Phys. C: Solid State Phys. **17**, 6039 (1984).

[31] G. Dresselhaus, Spin-orbit coupling effects in zinc blende structures, Phys. Rev. **100**, 580 (1955).

[32] D. Stein, K. von Klitzing, and G. Weimann, Electron Spin Resonance on $GaAs-Al_xGa_{1-x}As$ Heterostructures, Phys. Rev. Lett. **51**, 130 (1983).

[33] M. Dobers, K. von Klitzing, and G. Weimann, Electron-spin resonance in the two-dimensional electron gas of $GaAs-Al_xGa_{1-x}As$ heterostructures, Phys. Rev. B **38**, 5453 (1988).

[34] R. Meisels, I. Kulac, F. Kuchar, and M. Kriechbaum, Electron spin resonance of the two- dimensional electron system in $Al_xGa_{1-x}As/GaAs$ at subunity filling factors, Phys. Rev. B **61**, 5637 (2000).

[35] D. Stein, G. Ebert, K. von Klitzing, and G. Weimann, Photoconductivity on $GaAs - Al_xGa_{1-x}As$ heterostructures, Surf. Sci. **142**, 406 (1984).

[36] Y. B. Vasil'ev, S. D. Suchalkin, Yu. L. Ivanov, S. Ivanov, P. S. Kop'ev, and I. G. Savel'ev, Photoconductivity under the conditions of the quantum Hall effect, JETP Lett. **56**, 377 (1992).

[37] N. G. Kalugin, Yu. B. Vasilyev, S. D. Suchalkin, G. Nachtwei, B. E. Sagol, and K. Eberl, Dynamics of the far infrared photoresponse in quantum Hall systems, Phys. Rev, B **66**, 085308 (2002).

[38] K. Hirakawa, K. Yamanaka, Y. Kawaguchi, M. Endo, M. Saeki, and S. Komiyama, Far-infrared photoresponse of the magnetoresistance of the two-dimensional electron systems in the integer quantized Hall regime, Phys. Rev. B **63**, 085320 (2001).

[39] M. Pakmehr, C. Bruene, H. Buhmann, L. W. Molenkamp, A. V. Stier, and B. D. McCombe, Landau levels and spin splitting in the two-dimensional electron gas of a HgTe quantum well near the critical width for the topological phase transition, Phys. Rev. B **90**, 235414 (2014).

[40] F. F. Fang and P. J. Stiles, Effects of a tilted magnetic field on a two-dimensional electron gas, Phys. Rev. **174**, 823 (1968).

[41] S. Brosig, K. Ensslin, A. G. Jansen, C. Nguyen, B. Brar, M. Thomas, and H. Kroemer, InAs-AlSb quantum wells in tilted magnetic fields, Phys. Rev. B **61**, 13045 (2000).

[42] M. Pakmehr, A. Khaetski, B. D. McCombe, N. Bhandari, M. Cahay, O. Chiatti, S. F. Fischer, C. Heyn, and W. Hansen, The *g*-factor of quasi-two-dimensional electrons in InAs/InGaAs/InAlAs inserted channels, Appl. Phys. Lett. **107**, 082107 (2015).

[43] I. L. Aleiner and L. I. Glazman, Two-dimensional electron liquid in a weak magnetic field, Phys. Rev. B **52**, 11296 (1995).

[44] D. R. Leadly, R. J. Nicholas, J. J. Harris, and C. T. Foxon, Critical collapse of the exchange enhanced spin splitting in two-dimensional systems, Phys. Rev. B **58**, 13036 (1998).

[45] A. A. Kiselev, K. W. Kim, and E. L. Ivchenko, Zeeman effect in wurtzite-based and strained cubic heterostructures, Phys. Status Solidi B **215**, 235 (1999).

[46] A. A. Kiselev, E. L. Ivchenko, and U. Roessler, Electron *g* factor in one- and zero-dimensional semiconductor nanostructures, Phys. Rev. B **58**, 16353 (1998).

[47] Z. Wilamowski, H. Malissa, F. Schäffler, and W. Jantsch, *g*-Factor Tuning and Manipulation of Spins by an Electric Current, Phys. Rev. Lett. **98**, 187203 (2007).

[48] S. Datta and B. Das, Electronic analog of the electro-optic modulator, Appl. Phys. Lett. **56**, 665 (1990).

[49] H. Kroemer, The 6.1 A° family (InAs, GaSb, AlSb) and its heterostructures: A selective review, Phys. E (Amsterdam) **20**, 196 (2004), and references therein.

[50] Z. F. Ezawa, *Quantum Hall Effects: Field Theoretical Approach and Related Topics* (World Scientific, London, 2008).

[51] I. Vurgaftman, J. R. Meyer, and L. R. Ram-Mohan, Band parameters for III-V compound semiconductors, J. Appl. Phys. **89**, 5815 (2001).